Spectroscopy and Excited-State Dynamics of Methyl Ferulate in Molecular Beams

Ivan Romanov, Yorrick Boeije, Josene M. Toldo, Mariana Telles Do Casal, Mario Barbatti, Wybren Jan Buma

Spectroscopy and Excited-State Dynamics of Methyl Ferulate in Molecular Beams

Journal:	*The Journal of Physical Chemistry*
Manuscript ID	jp-2024-057923.R2
Manuscript Type:	Special Issue Article
Date Submitted by the Author:	16-Oct-2024
Complete List of Authors:	Romanov, Ivan; Universiteit van Amsterdam, Faculty of Science Boeije, Yorrick; University of Cambridge, Physics Toldo, Josene ; Aix-Marseille Université, Chemistry T. do Casal, Mariana; Katholieke Universiteit Leuven Faculteit Wetenschappen Barbatti, Mario; Aix-Marseille Universite, Institut de Chimie Radicalaire, UMR 7273 Buma, Wybren; Universiteit van Amsterdam, Faculty of Science

Spectroscopy and Excited-State Dynamics of Methyl Ferulate in Molecular Beams

Ivan Romanov,[†,⊥] Yorrick Boeije,[†,⊥] Josene M. Toldo,[‡] Mariana Telles do Casal,[‡,¶] Mario Barbatti,[‡,§] and Wybren Jan Buma[*,†,‖]

†*Van 't Hoff Institute for Molecular Sciences, University of Amsterdam, Science Park 904, 1098 XH Amsterdam, The Netherlands*

‡*Aix Marseille University, CNRS, ICR, 13397 Marseille, France*

¶*Department of Chemistry, Physical Chemistry and Quantum Chemistry Division, KU Leuven, 3001 Leuven, Belgium*

§*Institut Universitaire de France, 75231 Paris, France*

‖*Radboud University, Institute for Molecules and Materials, FELIX Laboratory, Toernooiveld 7c, 6525 ED Nijmegen, The Netherlands*

⊥*These authors contributed equally to this work.*

E-mail: w.j.buma@uva.nl

Abstract

The spectroscopic and dynamic properties of methyl ferulate –a naturally occurring ultraviolet-protecting filter– and microsolvated methyl ferulate have been studied under molecular beam conditions using resonance enhanced multiphoton ionization spectroscopy in combination with quantum chemical calculations. We demonstrate and rationalize how the phenyl substitution pattern affects the state ordering of the lower excited singlet state manifold and what the underlying reason is for the conformation-dependent Franck-Condon (FC) activity in the UV-excitation spectra. Studies on microsolvated methyl ferulate reveal potential coordination sites and the influence of such a coordination on spectroscopic properties. Our quantum chemical studies also enable us to obtain a quantitative understanding of the dominant excited-state decay routes of the photoexcited $\pi\pi^*$ state involving a $\sim$3 ns intersystem crossing pathway to the triplet manifold –which is much slower than found for coumarates– and a relatively fast intersystem crossing back to the ground state ($\sim$30 ns). We show that a common T_1/S_0 crossing can very well explain the observation that T_1 lifetimes are quasi independent of the phenyl substitution pattern.

1. Introduction

Molecules that absorb UV radiation are well known, both in natural and artificial forms. Their use can broadly be divided into compounds that are merely used to absorb photons such as found in sunscreens and other UV filters[1] to compounds in which the photon energy is converted into other targeted forms of energy such as chemical energy (photosynthesis)[2,3] or mechanical energy (molecular motors).[4,5] Less widely known applications focus on converting photon energy into thermal energy. Photon-to-heat conversion may be achieved indirectly through photochemical formation of strained products that release heat by a catalytic back-reaction.[6] Alternatively, direct photon-to-heat conversion from electronically excited states has started to attract considerable attention because of the potential of such so-called molecular heaters to boost crop growth, thereby addressing the increasing societal problem of food security.[7]

Cinnamates are a class of compounds widely used in nature as UV screening compounds.[1] As such, they represent a natural starting point for the further development of sunscreen components and molecular heaters. By now, a wide range of chemically modified cinnamates have been explored for their properties.[8–15] Such properties ideally involve a large UV absorption coefficient and fast internal conversion to the ground state without any long-lived electronically excited states. The latter requirement implies facile access to a real crossing between the potential energy surfaces of the electronically excited and the ground state, i.e., a conical intersection.[16–18] For a long time, coumarates employed in commercial sunscreens (2-ethylhexyl-4-methoxycinnamate (EHMC)) were assumed to fulfil such conditions. However, Tan *et al.* showed in 2014 that their excited-state dynamics also involve a long-lived electronically excited state[19] that was subsequently identified by Ebata *et al.* as being the lowest excited triplet state.[20] Such long-lived states are clearly detrimental to the efficacy of a sunscreen. As such, the study by Tan *et al.* prompted a renewed interest in the photochemical characterization of natural and artificial UV filters.[1,7,18,21–31]

Optimization –and ultimately a rational design– of novel cinnamate-based compounds

requires detailed insight into their spectroscopic properties and their excited-state dynamics, and in particular how these are modified by substitutions.[32] Initial studies revealed that these properties are delicately determined by the three lower-lying excited singlet states, the $V(\pi\pi^*)$, $V'(\pi\pi^*)$, and $^1n\pi^*$ states, with the $V(\pi\pi^*)$ state being the strongly allowed HOMO $\rightarrow$ LUMO excitation and the $V'(\pi\pi^*)$ state having a large HOMO $\rightarrow$ LUMO+1 character.[33] In coumarates, the $V(\pi\pi^*)$ and $V'(\pi\pi^*)$ states are nearly degenerate, with the $V'(\pi\pi^*)$ state being the lowest one for vertical excitation. Adiabatically, however, the $^1n\pi^*$ state becomes the lowest electronically excited singlet state.[34,35] This has important consequences as this state enables efficient intersystem crossing (ISC) to the triplet manifold.[36,37] On the other hand, in sinapates –which feature two meta-substituted electron-donating methoxy-groups– this order is completely reversed with the strongly allowed $V(\pi\pi^*)$ state being the lowest excited state for both vertical as well as adiabatic excitation.[12,29] Interestingly, the assignment to the $V(\pi\pi^*)$ state was originally made by comparing experimentally observed and computationally predicted Franck-Condon (FC) activity in the excitation spectrum.[12] Follow-up studies showed, however, that the structural relaxation in the excited state is highly conformer dependent.[38] Despite the energetic inaccessibility of the $^1n\pi^*$ state in sinapates, it was found that decay of the $V(\pi\pi^*)$ state may still proceed via ISC, although to a much lesser extent than in coumarates.[9,38]

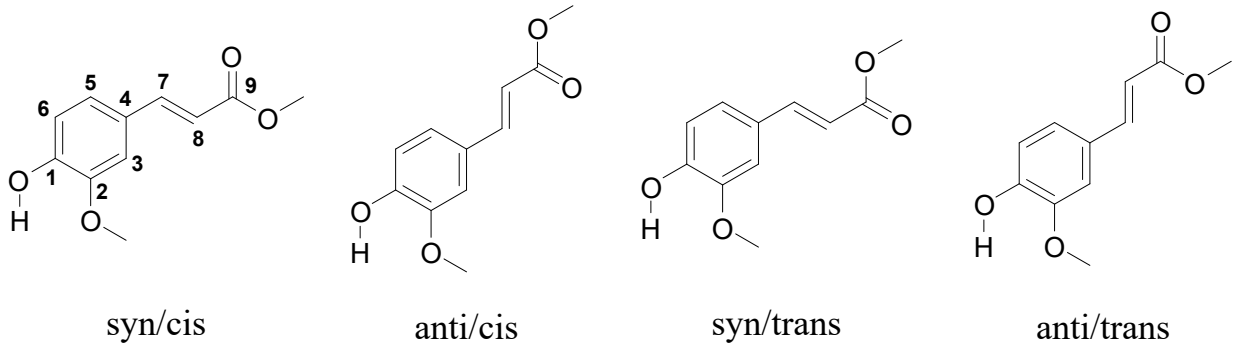

Scheme 1: Four lowest-energy stable conformers of methyl ferulate with atom labelling as used throughout the text. *Syn/anti* indicates the relative orientation of the O-H and C_7=C_8 bonds, while *cis/trans* refers to the relative orientation of the C_7=C_8 and C_9=O bonds.

Methyl ferulate (MF, Scheme 1) –which can be seen as coumarate with a single meta-substituted methoxy group instead of the two that are present in sinapates– is an ideal candidate to further our understanding of the influence of meta-substituted methoxy groups on the spectroscopic and dynamic properties of the lower electronically excited singlet states. A recent report on ferulic acid (FA) suggests that the triplet manifold is efficiently populated similar to coumarates, even though the $^1n\pi^*$ excitation energy was determined to be higher than those of the $V(\pi\pi^*)$ and $V'(\pi\pi^*)$ states.[9] Here, we present detailed experimental and quantum chemical studies of the UV excitation spectrum of MF and how these are influenced by solvation. These studies are complemented by IR-depletion spectra for further assignment of the specific conformation. We show that the vibrational activity in the excitation spectra of these conformers is delicately dependent on the molecular conformation. One should therefore be cautious with the assignment of the character of the electronically excited state on the basis of observed vibronic activity.

We also investigate in detail the decay pathways available to photoexcited MF, aiming to obtain not only a qualitative understanding of these pathways but also a quantitative agreement between experiment and theory. These studies provide insight into the ISC pathways of substituted cinnamates. Importantly, they also reproduce at a quantitative level experimental observations and thereby provide a consistent explanation for the observation that the decay rate of the lowest excited triplet state to the ground state is quasi-independent of the substitution pattern. All in all, these studies pave the way for a further rational optimization of cinnamates for applications as UV absorbers but also for their application in photothermal materials.

2. Methods

2.1 Experimental

Methyl ferulate was used as purchased from Sigma Aldrich. Resonance Enhanced Two Photon Ionization (R2PI), UV-UV depletion, IR-UV depletion, and pump-probe studies have been performed on a molecular beam setup described in detail before.[39] In these experiments methyl ferulate was heated to 140 °C in an *in situ* glass container just before the pulsed valve, and its vapor seeded into a supersonic expansion of 2.0 bar neon using a pulsed valve (General Valve Iota One) with an orifice diameter of 0.5 mm that was kept 5 °C higher in temperature to avoid clogging. Typically, a pulse duration of 180-220 µs was used. Because of the unavoidable presence of water vapor in gas tubes and the sample container itself, this expansion not only led to supersonically cooled methyl ferulate but also to clusters of methyl ferrulate with water. The molecular beam thus created was subsequently skimmed with a 2.5 mm skimmer and directed into the ionisation region, where mass-resolved ion detection was performed using a reflectron time-of-flight spectrometer (R.M. Jordan Co.).

One- and two-color Resonance Enhanced Two-Photon Ionisation (R2PI) experiments have been performed using a frequency-doubled Sirah Cobra-Stretch dye laser operating on DCM and pumped by a Spectra Physics Lab-190 Nd:YAG laser. In the two-color R2PI and pump–probe experiments, ionisation was performed with a Neweks PSX-501 ArF excimer laser (193 nm, 6.42 eV). To obtain non-saturated (1+1') excitation spectra, typical excitation energies of <10 µJ needed to be used, while typically ionization pulse energies of 0.05 mJ were employed to keep the one-color signal from the ionization laser as small as possible. Experiments focusing on low-intensity transitions in the excitation spectrum were performed in a one-color (1+1) scheme with typical pulse energies of 0.3 mJ. In pump-probe studies of the excited-state dynamics, the in analog mode detected ion yield at the molecular mass was monitored as a function of the delay between the excitation and ionization laser that was scanned using a Stanford Research Systems DG645 delay generator.

UV-UV depletion experiments have been performed by depopulating the ground state with a frequency-doubled Sirah Precision Scan dye laser operating on DCM and pumped by a Spectra Physics Lab-190 Nd:YAG laser. These experiments typically used pulse energies of 1.5-2 mJ for the depletion step and a time delay between the depletion laser and the excitation-ionization probe lasers of 150 ns. For the IR-UV depletion experiments, an IR pump beam in the range of 2870-3440 cm^{-1} and a typical pulse energy of 1 mJ was produced by difference frequency mixing the output of the Sirah Precision Scan dye laser operating on LDS 789 (779-815 nm) with the fundamental of the Nd:YAG laser in a $LiNbO_3$ crystal. This IR beam was partially focused by a lens with a focal length of 30 cm placed at a distance of 20 cm from the intersection with the molecular beam. The excitation-ionization probe lasers, on the other hand, were not further focused but reduced by pinholes to an appropriate size. In these experiments a typical time delay between depletion and probe lasers of 200 ns was employed.

2.2 Theoretical

Ground state geometries of MF and MF-H_2O conformers were optimized with Density Functional Theory (DFT) at the ωB97XD/cc-pVDZ level,[39,40] while Time-Dependent (TD)-DFT at the same level was employed to optimize geometries in electronically excited states. These geometries were subsequently used to determine vertical and adiabatic excitation energies for electronically excited singlet and triplet states using TD-DFT as well as the combined Density Functional Theory and MultiReference Configuration Interaction (DFT/MRCI)[40,41] method. TD-DFT excitation energies were computed at the ωB97XD/aug-cc-pVTZ level, while DFT/MRCI energies were obtained from DFT calculations at the BH-LYP/def2-TZVP level in combination with MRCI calculations. For the latter calculations, a modified set of the original empirical parameters[40] was used ($p_1 = 0.629$, $p_2 = 0.611$, $p_J = 0.119$, $p[0] = 8.000$, $\alpha = 0.503$) as suggested in Abiola *et al.*[7] In these calculations, the cut-off energy for the configuration selection was set to 1 Hartree to ensure that all relevant electronic

configurations would be included in the calculations.

Simulations of vibrationally-resolved excitation spectra have been performed by ωB97XD/cc-pVDZ (TD-)DFT calculations of the force fields in ground and electronically excited states followed by calculations of the pertinent Franck-Condon factors. For comparison with the experimental spectra theoretically calculated vibrational frequencies were scaled with a uniform scaling factor of 0.953.[42] (TD)-DFT calculations have been performed with the Gaussian16, Rev.A.03 suite of programs[43] except for the DFT/MRCI calculations for which the DFT part was calculated with the Turbomole 7.5.0 package.[44] The MRCI part was calculated using the parallelized version of the MRCI code.[45]

For the singlet states, scans of the potential energy curves were obtained using linearly interpolated intrinsic coordinates (LIIC). For the T_1 state, on the other hand, a relaxed surface scan was obtained in which interpolated geometries were optimized using unrestricted DFT (uDFT) while constraining the C_4-C_7=C_8-C_9 dihedral angle. Corresponding single-point singlet energies were computed at each geometry with ωB97XD/aug-cc-pVTZ TD-DFT calculations. Minimum energy surface crossings (MESX) between singlet states and between singlet and triplet states were computed using an in-house modified version of the CIOpt program developed by Levine and Martinez,[46] which employs a sequential penalty function to optimize state crossings without the need of nonadiabatic coupling vectors. Initial values for the penalty weight and smoothing parameter were set to 3.5 and 0.025 Hartree, respectively.

Spin-orbit coupling matrix elements (SOCMEs) were evaluated at several optimized structures, including the optimized triplet structures and T_1/S_0 MESX. Before the SOC calculation, TD-DFT single point energies were computed at the ωB97XD/aug-cc-pVTZ level with 6 d and 10 f basis functions and symmetry turned off. SOCME values were then obtained using the Breit-Pauli spin-orbit Hamiltonian with effective charge approximation[47] as implemented in the PySOC program.[48]

3. Results and Discussion

3.1 Spectroscopy methyl ferulate

Figure 1 displays the R2PI excitation spectrum of MF under non-saturated (a) and saturated (b) excitation conditions. The former excitation conditions have been employed to determine accurately the Franck-Condon (FC) factors for active vibrations and compare these with quantum chemical predictions. The latter, on the other hand, serve for comparing experimentally observed vibrational frequencies in the electronically excited state with theoretically predicted ones. As expected, these spectra are quite similar to the spectrum reported previously for ethyl ferulate (EF)[30] albeit that the EF spectrum –as also indicated in the previous study– was strongly saturated. In the study reported in ref.[30] two EF conformers were observed. Interestingly, UV-UV depletion spectroscopy on MF (Figures 1 (c), (e), and (g)) allows us to identify three species contributing to these spectra with 0-0 transitions at 31508.5, 31659.6, and 32083.7 cm^{-1}, and each displaying a dominant vibrational activity of a low-frequency bending mode similar to observed for EF.[30] The lowest-energy origin transition (31508.5 cm^{-1}) is close to the two origin transitions identified for EF (31491.1 and 31507.0 cm^{-1}).[30] Previous studies on the bare chromophore FA identified two conformers with origin transitions at 31780 and 32095 cm^{-1}.[9] Comparison with the *syn/cis* conformer of MF –which has the lowest excitation energy– thus leads to the conclusion that methylation of the carboxyl group leads to a red-shift of 271 cm^{-1}. It is interesting to notice that this is opposite to what is observed for coumaric acid[49] and sinapic acid[10] for which methylation leads to blue-shifts of 116 and 304 cm^{-1}, respectively.[19,29]

In the case of sinapic acid one of the arguments to assign the absorbing state as the $V(\pi\pi^*)$ state and not the $V'(\pi\pi^*)$ state was the observed Franck-Condon activity.[12] For the $V(\pi\pi^*)$ state quantum chemical calculations predicted an extensive C_4-C_7=C_8 bend progression, while for the $V'(\pi\pi^*)$ state such activity was predicted to be much smaller. The present study on MF shows, however, that such an argument should be used with caution as

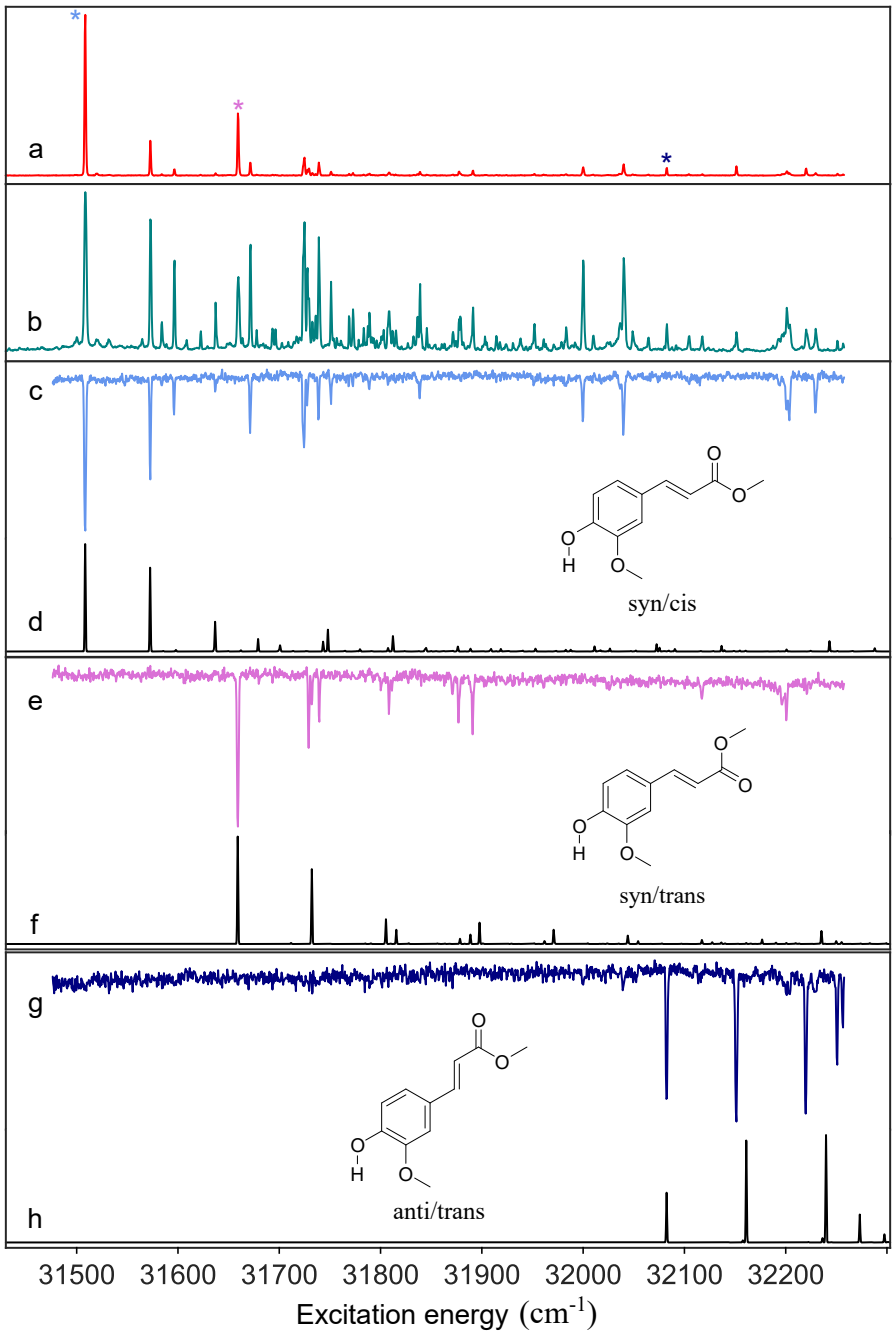

Figure 1: (1+1') R2PI (a) and (1+1) R2PI (b) excitation spectra of MF. UV-UV depletion spectra of three conformers depleted at 31508.5 cm^{-1} (c), 31659.6 cm^{-1} (e) and 32083.7 cm^{-1} (g) -indicated by asterisks in (a)- which are assigned to the *syn/cis*, *syn/trans*, and *anti/trans* conformations, respectively, based on the TD-DFT computed FC spectra depicted in (d), (f), and (h).

the depletion spectra of the two lowest-energy conformers (c and e) display limited C_4-C_7=C_8 bend activity leading to a "stairs" pattern (intensity distribution over the Franck-Condon progression with the 0-0 transition having the highest intensity), while for the highest-energy conformer (g) a "quartet" pattern (intensity distribution over the Franck-Condon progression with the 0-1 and 0-2 transitions having a higher intensity than the 0-0 and 0-3 transitions) with extensive activity of this mode is observed. We thus conclude that the Franck-Condon activity of the C_4-C_7=C_8 in-plane bending mode does not only depend on the nature of the excited state but also on the specific conformer.

Quantum chemical calculations enable us to obtain more insight into these observations and understand how the substitution pattern on the phenyl group affects the spectroscopic properties of these compounds. These calculations find four stable MF ground-state conformers (Scheme 1) with relative energies given in Table 1, noticing that the differences between the DFT and DFT/MRCI results are minor. Similar to previous conclusions on the stability of conformers of ethyl ferulate,[30] methyl sinapate,[29] ferulic acid,[9] and sinapic acid,[10] we find that the *syn/cis* conformer is the most stable one and will thus have the largest contribution to the R2PI spectrum in Figure 1a given that the predicted $V(\pi\pi^*)$ oscillator strengths of all conformers are approximately equal. For this reason, we focus first on the excited state properties of the *syn/cis* conformer before returning to the assignment of the individual conformers.

Table 1: Relative energies of MF conformers calculated at the ωB97XD/aug-cc-pVTZ DFT level and associated room temperature (RT) predicted population ratios.

Conformer	ΔE_{DFT} (kcal/mol)	RT Population	RT Population (Experimental)[a]
syn/cis	0	1	1
anti/cis	0.28	0.63	-
syn/trans	0.67	0.32	0.35
anti/trans	1.28	0.12	0.13

[a]Determined from integrated intensities of bending vibration progression bands

According to our DFT/MRCI calculations, the manifold of the lower electronically excited singlet states of the *syn/cis* conformer of MF is composed of three states which are ordered

according to their vertical excitation energies as $V(\pi\pi^*) < V'(\pi\pi^*) < {}^1\mathrm{n}\pi^*$ (Table 2). Such an ordering –although with slightly higher excitation energies– is found by TD-DFT calculations on MF (Table S1), as well as by TD-DFT calculations on FA.[9] CASPT2 calculations on EF predict that for vertical excitation the ${}^1\mathrm{n}\pi^*$ state is S_2.[30] Further comparative studies on EF and MF would thus be of interest, but are outside the scope of the present work.

Table 2: Vertical and adiabatic DFT/MRCI excitation energies (eV) of the lower-lying electronically excited singlet states of the *syn/cis* conformer of MF with oscillator strength of corresponding transition given in parentheses.

Transition	Vertical	Adiabatic
V($\pi\pi^*$)	4.02 (0.56)	3.81[a] (0.67)
V'($\pi\pi^*$)	4.40 (0.25)	4.22 (0.46)
${}^1\mathrm{n}\pi^*$	4.45 (4×10^{-4})	3.83 (6×10^{-5})

[a]Experimental adiabatic excitation energy is 3.91 eV

The $V(\pi\pi^*)$ state is described by a pure HOMO $\rightarrow$ LUMO transition (Figure 2 and Table S2) and has a much larger oscillator strength than the configurationally mixed $V'(\pi\pi^*)$ and ${}^1\mathrm{n}\pi^*$ states. Inspection of the molecular orbitals rationalizes why the $V(\pi\pi^*)$ state is red-shifted with respect to MC, as the methoxy group in the ortho position raises the energy of the HOMO but does not affect the LUMO due to the non-bonding character at the ortho position. The large oscillator strength of the $\mathrm{S}_0 \rightarrow V(\pi\pi^*)$ transition arises from the spatial overlap between the HOMO and LUMO in combination with a relatively small charge transfer from the phenyl ring to the carbonyl tail accompanying the transition (see electronic difference density (EDD) maps in Figure 2). These EDD maps show that excitation of the $V(\pi\pi^*)$ state also leads to transfer of electron density from the C_7=C_8 to the C_4-C_7 regions, which thereby acquire less and more double bond character, respectively. Similar to the $V(\pi\pi^*)$ state, π-electronic density is transferred upon excitation of the $V'(\pi\pi^*)$ state from the phenyl moiety to the C_4-C_7 region. It is noteworthy that the EDD maps of the $V(\pi\pi^*)$ and the $V'(\pi\pi^*)$ states also show significant differences in the phenyl ring arising from the differences in electron distribution in the HOMO and HOMO-1 orbitals. Finally, the EDD map for excitation of the $n\pi^*$ state shows how electron density from the oxygen lone pair is

displaced to the π-plane, in particular the acrylate region.

Geometry relaxation of the molecule in these three electronically excited states lowers the energy of the $^1n\pi^*$ state significantly. Nevertheless, its adiabatic excitation energy is still higher than that of the bright $V(\pi\pi^*)$ state (Table 2). As a result, the three states adiabatically become ordered as $V(\pi\pi^*) < {}^1n\pi^* < V'(\pi\pi^*)$. Similar to MS we thus find that the $V(\pi\pi^*)$ state of *syn/cis* MF is both vertically as well as adiabatically S_1, as opposed to MC, where the $^1n\pi^*$ state is adiabatically the lowest excited singlet state.[19] Both the predicted excited state ordering as well as the large oscillator strength of the $V(\pi\pi^*)$ state leads us to the conclusion that the excitation spectrum observed in Figure 1 is associated with the $V(\pi\pi^*)$ state.

Our DFT/MRCI calculations predict that for the *syn/trans* and *anti/trans* conformers the $^1n\pi^*$ state is adiabatically slightly lower in energy than the $V(\pi\pi^*)$ state (Table S3), which is in contrast with the TD-DFT calculations that predict that adiabatically the $^1n\pi^*$ state is at a significantly higher energy (Table S1). We contend, however, that for the present experiments it is not of direct importance whether the $^1n\pi^*$ state is adiabatically above or below the $V(\pi\pi^*)$ state. In our experiments we excite adiabatically a strongly-allowed electronically excited state, which thus must be a $\pi\pi^*$ state. Internal conversion to the $^1n\pi^*$ state is expected to be slow as the energy barrier that must be overcome will be quite high because of the large differences in equilibrium geometry of the two states. Previous calculations find indeed that the CI between the $V(\pi\pi^*)$ and $^1n\pi^*$ states, which would accelerate such an internal conversion process, is more than 0.5 eV above the minimum of the $V(\pi\pi^*)$ state.[30] We thus conclude that for all conformers the excitation spectrum observed in Figure 1 is associated with the $V(\pi\pi^*)$ state.

Such an assignment is further supported by the calculated vibrationally resolved excitation spectra (Figures 1 (d), (f), (h)), which for the $V(\pi\pi^*)$ state show a similar vibronic activity as observed experimentally. What is important to notice is that the observed "stairs" Franck-Condon patterns of the lowest-energy conformers (Figures 1 (c) and (e)) are re-

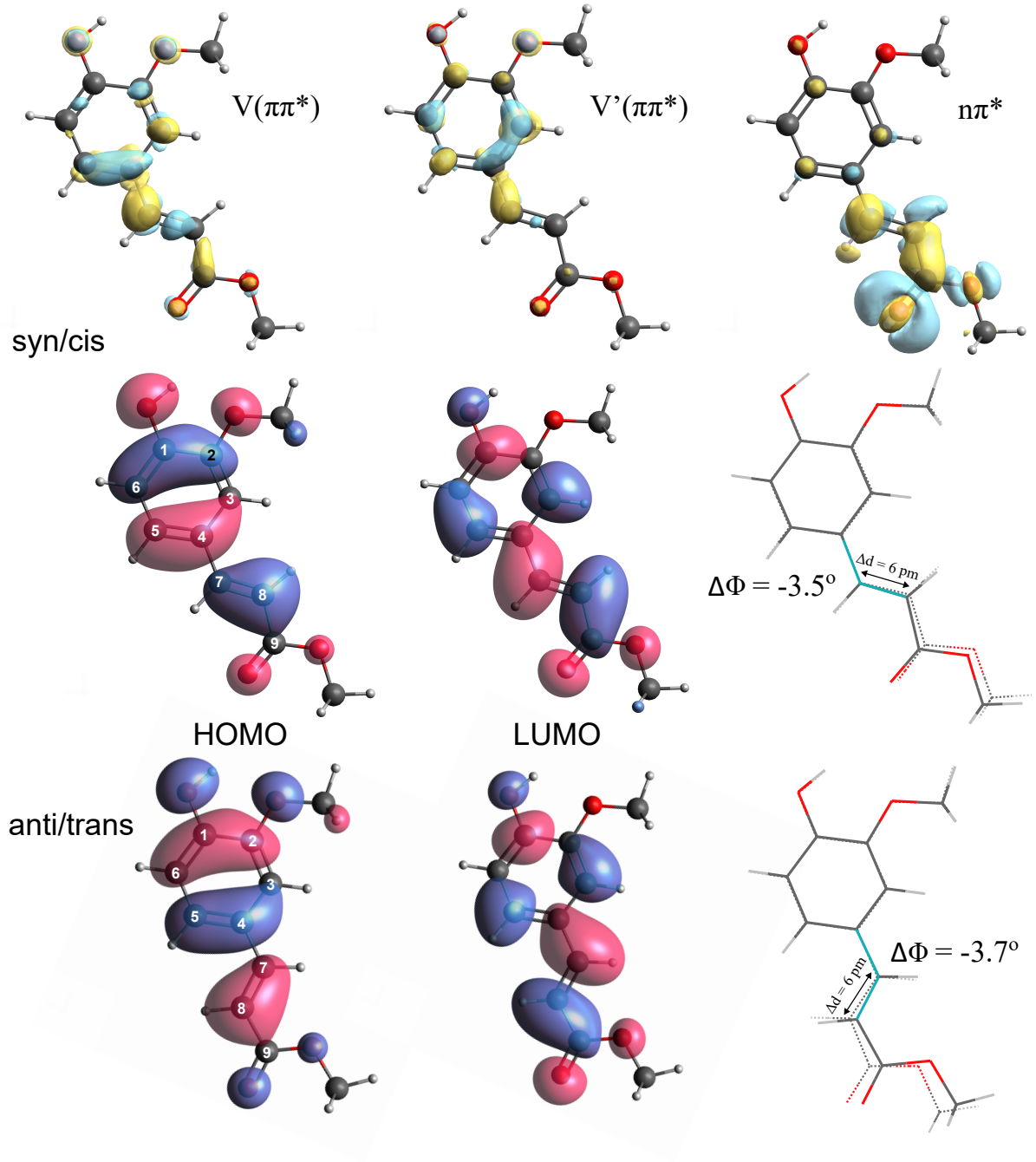

Figure 2: Top: Electron density difference (EDD) maps for the $V(\pi\pi^*)$, $V'(\pi\pi^*)$ and ^{1}nπ^* states of the *syn/cis* conformer of MF with blue and yellow indicating hole and electron density, respectively. Middle and bottom panels show Kohn-Sham HOMO and LUMO orbitals for *syn/cis* and *anti/trans* conformers, respectively. The right structures indicate the change of the C_4-C_7=C_8 angle Δ in the $V(\pi\pi^*)$ state of the *syn/cis* (middle) and *anti/trans* (bottom) conformers compared to the ground state.

produced computationally for the $V(\pi\pi^*)$ excitation spectra of the *syn/cis* and *syn/trans* conformers, as well as the "quartet" pattern found in the $V(\pi\pi^*)$ excitation spectra of the *anti/cis* and *anti/trans* conformers (see Figure S1 for predicted spectrum of *anti/cis*). Moreover, for the latter two conformers the Franck-Condon patterns calculated for excitation of the $V'(\pi\pi^*)$ state are in stark contrast with what is observed experimentally (Figure S2), thereby excluding the possibility that for these conformers the $V'(\pi\pi^*)$ state is adiabatically the lowest excited singlet state.

The above considerations, in combination with the calculated population ratios, lead to the conclusion that the depletion spectra in Figures 1(c) and 1(e) should be assigned to the *syn/cis* and *syn/trans* conformers, respectively. Such a conclusion is in agreement with the lower adiabatic excitation energy predicted for the former. Based on the "quartet" pattern observed in the depletion spectrum of Figure 1(g), the same considerations lead one, however, also to conclude that this spectrum should be assigned to one of the *anti* conformers. The low intensity of the 32083.7 cm^{-1} band and the experimentally measured C_4-C_7=C_8 bend frequency (69 cm^{-1}) –which is closer to the frequency predicted for the *anti/trans* conformer (73 cm^{-1}) than for the *anti/cis* conformer (62 cm^{-1})– would tend to favor an assignment to the *anti/trans* conformer. Such an assignment implies, however, also that the *anti/cis* conformer, which is predicted to be the one-but-most stable conformer, is absent in our experiments. Rotationally-resolved excitation spectra or ground-state rotational spectroscopy could, in this respect, allow to come to a conclusive assignment.

Given the conclusion that the *syn* and *anti* conformations display distinct Franck-Condon activity of the C_4-C_7=C_8 bending mode while previously it was assumed that these differences indicate excitation of different electronic states, it is of interest to further understand the underlying reasons for these distinct Franck-Condon activities. The excited-state displacements associated with these activities can qualitatively be understood by inspection of the HOMO and the LUMO (Figure 2). These show for the HOMO of the *syn/cis* conformer an antibonding interaction between the π orbitals of C_3 and $C_{7/8}$ while for the LUMO part

of this antibonding interaction is replaced by a bonding interaction. A HOMO → LUMO excitation will thus favour a reduction of the C_4-C_7=C_8 angle, or, in other words, induce Franck-Condon activity in the pertaining normal mode. For the HOMO of the *anti* conformers, on the other hand, the antibonding interaction between the π orbitals of C_5 and $C_{7/8}$ is larger than the antibonding interaction between the π orbitals of C_3 and $C_{7/8}$ in the *syn* conformers (Figure 2). As a result, an increased Franck-Condon activity is to be expected in the C_4-C_7=C_8 bending mode as is indeed observed experimentally. A similar conclusion is drawn when the steric interactions between H_8 and H_3 and between H_7 and H_4 in the *syn* conformers are compared with the analogous interactions between H_7 and H_5 and between H_4 and H_8 in the *anti* conformers since the latter distances are smaller than the former. Both aspects (interactions between π orbitals and steric interactions between H atoms) thus favour a larger activity of the C_4C_7=C_8 bending mode in the excitation spectrum of the *anti* conformers.

The above observations indicate that one should be cautious when assigning the electronic nature of the excited state based on the Franck-Condon activity of a single conformer, in particular when there is an asymmetric substitution in the phenyl ring. In contrast, in MC and MS, where the phenyl ring is symmetrically substituted, it might very well be that the *anti/syn* Franck-Condon distinction is less pronounced.[12] In this respect it is interesting to notice that for MS it has been concluded that excitation of the $V(\pi\pi^*)$ state is accompanied by a larger change in the C_4-C_7=C_8 angle than in MF, and that this change is larger for the *syn/cis* conformer than for the *anti/cis* conformer.[38]

3.2 Influence of solvation on spectroscopy of methyl ferulate

The R2PI spectrum of microsolvated MF obtained at the mass of the MF-H_2O molecular ion is shown in Figure 3. The lowest-energy band in this spectrum is observed at 30977.5 cm^{-1}, implying that the coordination of a water molecule redshifts the lowest excitation energy observed for MF (Figure 1) by 531 cm^{-1}, which is less than observed in MS (822

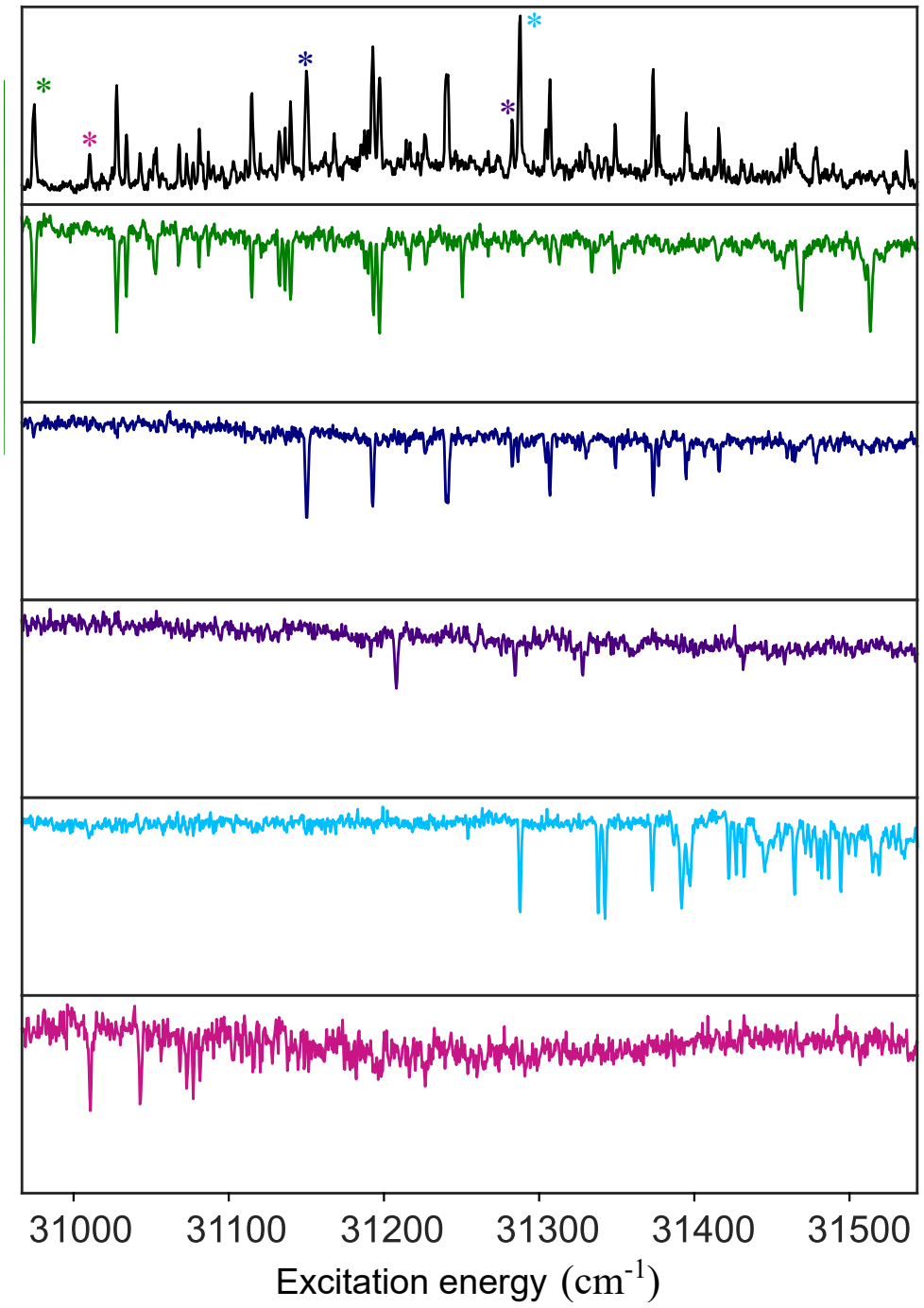

Figure 3: 1+1' R2PI spectrum (black) and UV-UV depletion spectra of MF-H_2O depleted at excitation energies of 30978 cm^{-1} (green), 31153 cm^{-1} (dark blue), 31211 cm^{-1} (purple), 31290 cm^{-1} (light blue), and 31014 cm^{-1} (pink) indicated with corresponding stars in R2PI spectrum.

cm^{-1})[29] and MC (641 cm^{-1}).[34,35,50] UV-UV depletion spectroscopy enables the identification of five MF-H_2O structures (Figure 3). These spectra inevitably show more complicated vibronic progressions than uncoordinated MF because of the additional intermolecular MF-H_2O vibrational modes.

In order to assign these spectra to specific MF-H_2O structures, IR-UV depletion spectroscopy has been applied (Figure 4). IR-UV depletion spectra obtained for conformers of the bare MF molecule (Figure S3) serve, in this respect, as a starting point for further comparisons. These spectra show for the *syn/cis* and *anti/trans* conformers a strong OH stretch absorption band at the same frequency (3591.8 and 3591.6 cm^{-1}, respectively) and at a slightly lower frequency (3590.6 cm^{-1}) for the *syn/trans* conformer. For MF-H_2O we expect two additional OH bands. The light blue and pink spectra in Figure 4 show, however, more than three bands. We attribute these additional bands to either combination bands or arising from excitation of more than one conformer at the employed UV probe wavelength.

The IR spectra of the microsolvated conformers reveal two new OH stretching mode bands, one at a much higher frequency (ν_3) than the OH stretching frequency of bare MF (ν_2), and one at a much lower frequency (ν_1) (see Table 3). For four of these conformers (green, dark blue, purple, and light blue traces in Figure 4), a band is observed close to the OH stretch band of the bare molecule, implying that H_2O coordination only mildly perturbs the MF OH stretching mode. We therefore assign these conformers to clusters designated as *carb* coordinated water clusters (Scheme 2) in which a water molecule is coordinated to the carbonyl group, similar to how water is coordinated in MS-H_2O clusters.[38] The pink trace, on the contrary, does not show an IR band close to the bare MF OH stretch frequency, indicating that coordination takes place with the phenolic OH. Such a coordination disrupts the intramolecular hydrogen bond between the OH and OCH_3 groups in the bare molecule, and replaces it with a weaker hydrogen bond of the phenolic OH with water. As a result, the Ph-OH stretch is blue shifted by $\sim$112 cm^{-1}.

With the exception of the carrier of the pink trace (thereafter referred to as the pink

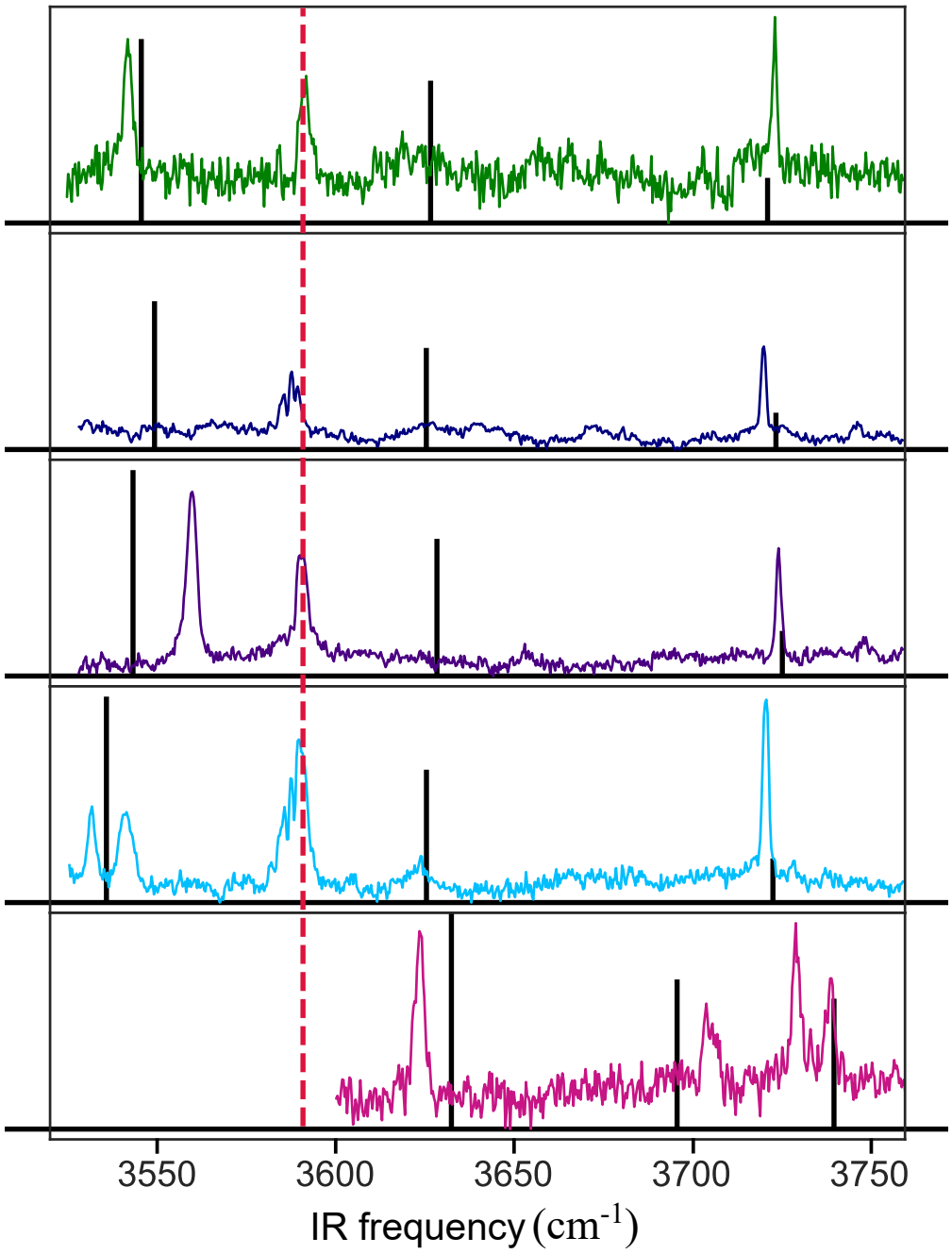

Figure 4: IR-UV depletion spectra of MF-H_2O conformers. The colored spectra match the conformers found in the UV-UV depletion spectra from Figure 3. Red dashed line indicates the frequency measured for the Ph-OH stretch in bare MF conformers (Figure S3). Calculated (normalized) IR spectra for the ground state of the assigned water cluster conformers are represented by black stick spectra (Table 3).

conformer), all conformers have the highest-frequency band (ν_1) around 3720-3730 cm^{-1}. The similar frequency of this band for the four different conformers suggests that it is associated with the non-hydrogen-bonded OH stretch of coordinated H_2O. It is interesting to notice that for MC-H_2O clusters –in which water is coordinated to the phenolic OH– this band is found at 3743 cm^{-1}.[36] Such a higher frequency is in line with the stronger hydrogen bond between the phenolic OH and H_2O compared to the hydrogen bond between C=O and H_2O. As such, it provides a further confirmation of the coordination site of water in these four conformers. The observation that for the pink conformer the highest-frequency band is found at 3739 cm^{-1} further corroborates our conclusion that in this conformer water is coordinated to the phenolic OH. In line with an assignment of the lowest-frequency band (ν_1) to the hydrogen-bonded OH stretch of coordinated water, much larger variations are observed for the lowest-frequency band (ν_1) of these four conformers. The stronger interaction of the bond with MF results in a reduction of its frequency and makes the frequency of this mode more susceptible to small variations in bonding characteristics.

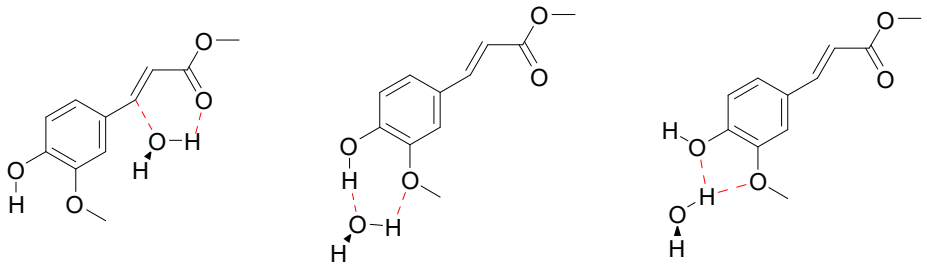

Scheme 2: A selection of possible relevant MF-H_2O structures of microsolvated MF clusters. Microsolvated MF-H_2O structures that differ in water coordination site are formally structurally isomers. For sake of simplicity, we will, however, refer to such isomers as conformers. Relative energies are given in Table S4. Possible hydrogen-bond interactions are indicated with red dashed lines.

Our calculations suggest for the structure of the pink conformer (Figure 4) two possible ways of coordinating a water molecule to the phenolic OH, which will be designated as *phen* and *phen2* (see Scheme 2). From an energy point of view, the *phen* coordination would

appear to be the most logical candidate (Table S4). Such an assignment is contradicted, however, by calculated IR spectra, which predict a phenolic OH stretch significantly red-shifted from the non-complexed molecule ($\sim$44 cm^{-1}) and a hydrogen-bonded OH stretch of water around $\sim$3340 cm^{-1} (Table S5). In contrast, the IR spectrum observed for the purple conformer displays a blue-shifted phenolic OH stretch and no bands at lower frequencies. IR spectra predicted for the *anti/cis_phen2* and *syn/cis_phen2* conformations, on the other hand, show a blue-shifted phenolic OH stretch and water OH stretch frequencies that nicely match experimentally observed bands (Table 3). Apparently, during the molecular beam expansion *phen2* conformers are produced that are subsequently kinetically trapped. An interesting question that remains is, however, why *phen* conformers are not observed. Although an unambiguous assignment to either of these two *phen2* conformers is not possible on the basis of the observed IR spectrum, predicted adiabatic excitation energies (Table S6) and Franck-Condon activities tend to slightly favour *syn/cis_phen2*.

Above we have concluded that the green, dark blue, purple and light blue traces in Figure 4 are associated with *carb* coordinated water clusters. On the basis of the calculated adiabatic excitation energies (Table S6) of each of the MF-H_2O conformers, these traces would be assigned to the *anti/cis_carb*, *syn/cis_carb*, *anti/trans_carb*, and *syn/trans_carb* conformers, respectively. Such an assignment is supported by the calculated ground-state energies of these conformers, which would lead to population ratios (Table S4) that qualitatively follow the intensities observed in the experimental excitation spectrum (Figure 4). Although not completely unambiguous, the experimental IR spectra are also in line with this assignment: (i) the *syn/trans_carb* conformer is predicted to have the lowest ν_1 frequency as is indeed observed in the light blue spectrum; (ii) the *syn/cis_carb* conformer is similarly predicted to have a lower ν_1 frequency as observed in the dark blue spectrum; (iii) the experimental IR spectrum of bare *anti/cis* MF is not known. The observation that the green spectrum is the only spectrum in which the ν_2 band is blue-shifted with respect to the Ph-OH frequencies measured for bare MF conformers thus suggests that it is associated with the *anti/cis_carb*

Table 3: DFT calculated and measured IR-UV OH stretch frequencies (cm^{-1}) for *carb* water clusters and *phen2* water clusters (Scheme 2). ν_1 represents the hydrogen-bonded OH stretch of coordinated H_2O, ν_2 the PhOH stretch, and ν_3 the non-hydrogen-bonded OH stretch of coordinated H_2O. Values in parentheses at ν_2 indicate the shift in wavenumbers with respect to the PhOH stretch of bare MF. ν' values denote experimental frequencies obtained by IR-UV depletion spectroscopy. The "Color" graph corresponds to line colors used in Figure 4

carb cluster	ν_1	ν_2	ν_3	Color	ν_1'	ν_2'	ν_3'
anti/cis	3545.6	3626.8 (+34.9)	3721.4	Green	3541.8	3591.9 (-)	3723.5
syn/cis	3549.3	3625.6 (+33.7)	3723.8	Dark blue	-	3587.8 (-4.0)	3720.4
anti/trans	3543.3	3628.6 (+36.7)	3725.6	Purple	3559.9	3590.7 (-0.9)	3724.5
syn/trans	3535.8	3625.7 (+33.8)	3722.9	Light blue	3531.8*	3589.8 (-0.8)	3721.0
phen2 cluster							
anti/cis	3633.1	3695.1 (+103)	3740.2	Pink***	3623.7	3704.2 (+112)	3739.3**
syn/cis	3632.7	3696.0 (+104)	3740.1				

* Another peak appears at 3541.4 cm^{-1}

** Another peak appears at 3729.3 cm^{-1}

*** Experimental frequencies can be assigned to either *anti/cis* or *syn/cis phen2* configuration.

conformer.

3.3 Excited-state dynamics of methyl ferulate

After excitation of MF to the $V(\pi\pi^*)$ state, several radiative and nonradiative decay pathways can bring the excited molecule back to the ground state. To elucidate these excited-state dynamics, pump-probe R2PI experiments have been performed. In these experiments, the vibrationless level of the $V(\pi\pi^*)$ state of a particular conformer is excited and subsequently ionized after a chosen delay. Figure 5 displays such pump-probe traces for the three identified conformers of MF. These traces have been analyzed by taking a Gaussian profile with

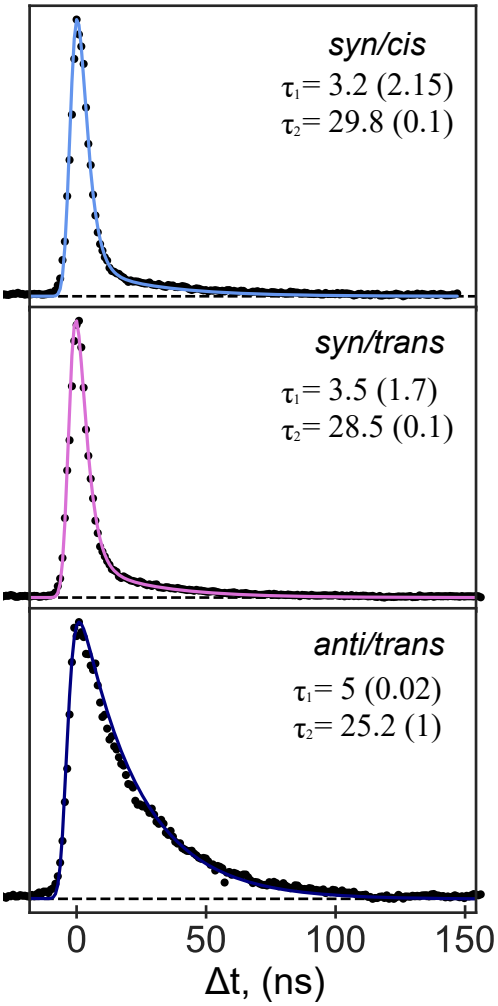

Figure 5: Time-resolved (1+1') R2PI decay curves after excitation of the vibrationless level of the $V(\pi\pi^*)$ state of the *syn/cis*, *syn/trans* and *anti/trans* conformations of methyl ferulate. The solid lines are bi-exponential fits convoluted with a Gaussian profile with decay times in ns, and relative amplitude of each component given in parentheses.

a width of about 6 ns as the cross-correlation of the two laser beams, and convoluting this profile with a multiexponential decay. Such an analysis leads to the conclusion that the decay features a short-time (τ_1 = 3-5 ns) as well as a long-time (τ_2 = 25-30 ns) component, indicating that two states are ionized within the resolution of the laser pulse, one of which is longer-lived than the other. As we have concluded that the $V(\pi\pi^*)$ state is adiabatically the lowest excited singlet state, we attribute the long-lived component to the decay of a triplet state. Considering that internal conversion from T_n to T_1 is expected to take place on a ps timescale, one can safely assume that the long-lived state is the lowest excited triplet state T_1. In general, one would expect a much longer lifetime for the lowest triplet state, but the short lifetimes observed here for MF nicely follows the triplet lifetimes observed in other cinnamate-based systems.[5,29,31,51]

Interestingly, all these cinnamate-based compounds -including now MF- display very similar lifetimes for the long-lived component[8,9,19,20,29,31,34,37,50] (20 to 30 ns). Moreover, for all practical purposes this lifetime is independent of the specific conformer considered, suggesting an underlying decay mechanism that is common to all these compounds. In the following, we aim to come to a fundamental understanding of this mechanism, not only qualitatively, but in particular also aim to obtain quantitative agreement between predicted and observed decay rates. To this purpose, we focus in the first instance on understanding the decay pathways of the V($\pi\pi^*$) state of the *syn/cis* conformer of MF by considering (i) fluorescence, (ii) internal conversion (IC), and (iii) intersystem crossing (ISC). We estimate the radiative lifetime from Fermi's golden rule given by

$$k_{\mathrm{rad}} = \frac{2\pi e^2 \nu^2}{\epsilon_0 m_e c^2} f \tag{1}$$

where e, ϵ_0, m_e, and c are the elementary charge, the vacuum electric permittivity, the mass of the electron, and the speed of light, respectively. Using the DFT/MRCI computed oscillator strength of 0.56, we obtain a radiative lifetime of 2.7 ns, which is close to the measured pump-probe lifetime of 3.2 ns. We thus conclude that radiative processes cannot

be excluded from considerations on the decay paths of the V($\pi\pi^*$) state.

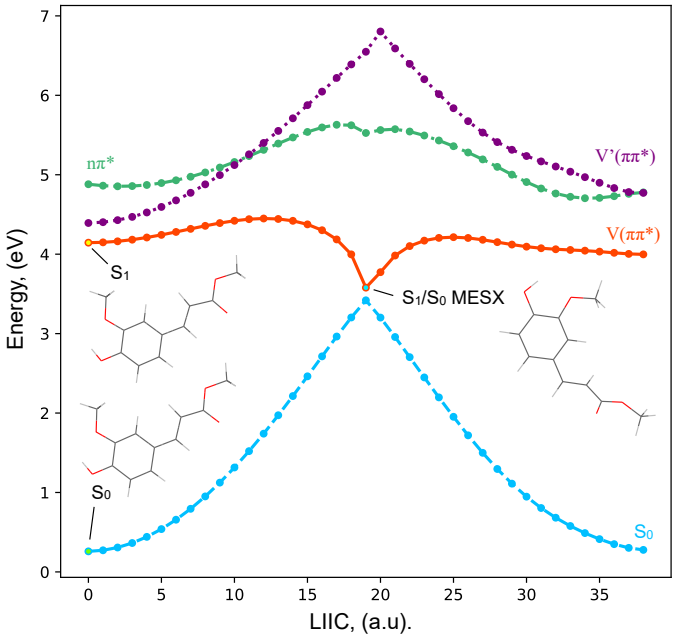

Figure 6: Potential energy profiles calculated at the TD-DFT/cc-pVDZ level of the ground and lower electronically excited singlet states of the *syn/cis* conformer of MF. The LIIC connects the equilibrium geometry of the $V(\pi\pi^*)$ state of the C_7=C_8 E isomer to the S_1/S_0 crossing and from there to the equilibrium geometry of the $V(\pi\pi^*)$ state of the C_7=C_8 Z isomer.

One of the nonradiative processes of the $V(\pi\pi^*)$ state that might contribute to the overall decay is internal conversion to S_0. Since the vibrational overlap between the vibrationless level of the $V(\pi\pi^*)$ state and isoenergetic vibrational levels in S_0 is very small, a contribution to internal conversion from the equilibrium geometry of the $V(\pi\pi^*)$ state is expected to be negligible. On the other hand, in regions where the energy gap between the potential energy surfaces of two states is small, internal conversion rates could become appreciable. Calculations for MF indeed show a surface crossing between these two states for a twisted geometry along the C_4-C_7=C_8-C_9 dihedral angle (Figure 6). However, considering the LIIC potential energy curve connecting the $V(\pi\pi^*)$ and the S_1/S_0 MESX, one finds that such a path is associated with a signification energy barrier (2455 cm^{-1}), which is much larger than the available thermal energy (7 cm^{-1}). We therefore conclude that this pathway is not accessible under our adiabatically cooled gas-phase conditions. At the same time, we notice

that this pathway might come into play under room-temperature solution conditions where much higher internal energies are available and where generally excitation at the absorption maximum takes place.

Finally, we consider intersystem crossing from the V($\pi\pi^*$) state to the triplet manifold. We model such a process using semi-classical Marcus theory, from which the ISC rate can be calculated[52] as follows:

$$k_{\mathrm{ISC}} = \frac{2\pi}{\hbar}|H_{\mathrm{SO}}|^2 \frac{1}{\sqrt{4\pi\lambda k_B T}} \exp\left(-\frac{(\lambda + \Delta E_{ST})^2}{4\lambda k_B T}\right) \quad (2)$$

where H_{SO} is the spin-orbit coupling matrix element between singlet and triplet states under consideration, λ the reorganization energy, and ΔE_{ST} the energy gap between the optimized singlet and triplet states involved in the ISC process (Figure S4), while k_B and T denote the Boltzmann constant and absolute temperature, respectively. λ corresponds to the energy difference between the triplet state energy at the optimized V($\pi\pi^*$) geometry (E_{T_nV}) and the energy of the optimized triplet state (E_{T_n}). In the present case, several potential final triplet states T_n need to be considered, which include the T_1 (V($^3\pi\pi^*$)), T_2 (V'($^3\pi\pi^*$)), and T_5 (^{3}nπ^*) states of which the equilibrium geometries are shown in Figure S4. Apart from these states, two more $\pi\pi^*$ triplet states fall within the relevant energy range designated as $T_3(^3\pi\pi^*)$ and $T_4(^3\pi\pi^*)$. Geometry optimization of the $T_3(^3\pi\pi^*)$ state was not possible as root switching with the V'($^3\pi\pi^*$) state occurred. Geometry optimization of the $T_4(^3\pi\pi^*)$ state, on the other hand, led to the structure depicted in Figure S4.

Table 4 reports for each of these states the parameters needed to calculate the ISC rate from S_1 to the pertinent triplet state. In order to assess the geometry dependence of the SOC matrix element we have calculated H_{SO} at both the equilibrium geometry of S_1 as well as at the equilibrium geometry of T_n. Table 4 shows that for the majority of the ISC pathways there is indeed a non-negligible geometry dependence of H_{SO} and k_{ISC}. In order to obtain the correct ISC rate, one would therefore need to incorporate this geometry dependence in the coupling matrix element between the initial and final Born–Oppenheimer states, which

would exclude a semi-classical Marcus theoretical approach. In the following we will therefore base our discussion on the predicted ISC rates assuming that the appropriately calculated rate would be in the range of values found by the calculations at the equilibrium geometry of S_1 and T_n.

Table 4: Marcus parameters and ISC rate for $V(\pi\pi^*) \rightarrow T_n$ transition based on Equation 2. Energies calculated with DFT/MRCI. SOCMEs and rates computed at 10 K evaluated at $V(\pi\pi^*)$ equilibrium geometry with in parentheses corresponding numbers evaluated at T_n equilibrium geometry.

State	$\langle V(\pi\pi^*)\|H_{\mathrm{SO}}\|T_n\rangle$ (cm^{-1})	$-\Delta E_{\mathrm{ST}}$ (eV)	λ (eV)	$(k_{\mathrm{ISC}})^{-1}$ (ns)	R2PI τ_1 (ns)
T_4	0.2 (0.2)	0.292	0.288	-	-
$T(n\pi^*)$	21.9 (13.9)	0.249	0.739	10^{18} (10^{18})	-
T_2	0.4 (0.09)	0.177	0.237	4 (83)	3.2
$T_{1,\mathrm{tw}}$	2.9 (0.08)	1.432	-0.033	-	-

As expected on the basis of El-Sayed rules for intersystem crossing,[53] the spin-orbit coupling between the V($\pi\pi^*$) and $^3n\pi^*$ states is relatively large. The ISC rate between these two states is nevertheless found to be very small because of the large difference between ΔE_{ST} and the reorganization energy λ. On the other hand, despite the small spin-orbit coupling between the V($\pi\pi^*$) and T_2 states, a relatively large rate is found for transitions between these two states. As a result of the distortion of the T_2 state along a symmetry-lowering hydrogen out-of-plane (HOOP) coordinate (see side view of T_2 in Figure S4), the V($\pi\pi^*$) $\rightarrow T_2$ transition is associated with a large λ that compensates for the large ΔE_{ST}. Table 4 shows that based on the calculated parameters, an ISC rate of (4-80 ns)$^{-1}$ is predicted, which is in reasonable agreement with the pump-probe lifetime of 3.2 ns measured for the *syn/cis* conformer. The same table shows that for the remaining two ISC channels to the T_1(V($^3\pi\pi^*$)) and T_4($^3\pi\pi^*$) states extremely small ISC rates are predicted. We thus come to the conclusion that ISC between the S_1 V($\pi\pi^*$) and T_2 states is by far the dominant relaxation channel among the possible singlet-triplet relaxation channels with a rate that is in quantitative agreement with our experimental observations.

We conclude this part of the discussion with a further comment on the differences between

the pump-probe traces of the *syn/cis* and *syn/trans* conformers and the pump-probe trace of the *anti/trans* conformer (Figure 5). The latter distinguishes itself by the small contribution of τ_1 compared to the former ones. Since τ_1 is in all cases similar, this excludes an explanation based on differences in ISC rate. An alternative explanation might be that contributions from radiatiative and/or nonradiative transitions from V($\pi\pi^*$) to S_0 are different. The observation that similar oscillator strengths are calculated for the V($\pi\pi^*$) $\rightarrow S_0$ transition of each conformer (0.67 for *syn/cis* and *anti/trans*, 0.68 for *anti/cis* and 0.66 for *syn/trans*) suggests that for the *anti/trans* conformer the V($\pi\pi^*$) $\rightarrow S_0$ nonradiative decay rate is signficantly smaller than for the other two conformers.

After ISC of V($\pi\pi^*$) to T_2, rapid internal conversion to the lowest excited triplet state T_1 takes place. The final step that brings the molecule back to its electronic ground state is the spin-forbidden $T_1 \rightarrow S_0$ transition, which occurs at a rate of $(30\ \text{ns})^{-1}$. We now aim to understand how this process can be relatively fast and why it is similar for all cinnamate-based systems studied so far. To this purpose, we consider once again the expression for the ISC rate derived from semi-classical Marcus theory (*vide supra*). Our calculations find -analogous to previous calculations on other cinnamate-based systems[8]- an MESX between T_1 and S_0. Under such conditions, the exponential term in the semi-classical Marcus theory expression can be replaced with the activation energy $\Delta E^{\ddagger}$ -the energy difference between the T_1/S_0 MESX and the energy E_{T_1} of T_1 at its equilibrium geometry (see Figure S4)- leading to the expression

$$k_{\text{ISC}} = \frac{2\pi}{\hbar}|H_{\text{SO}}|^2 \frac{1}{\sqrt{4\pi\lambda k_B T}} \exp\left(-\frac{\Delta E^{\ddagger}}{k_B T}\right) \tag{3}$$

One further difference with the original expression is that $\hat{H}_{\text{SO}}$ is now computed at the T_1/S_0 MESX geometry.

Figure 7 displays the relaxed T_1 surface scan along the C_4-C_7=C_8-C_9 dihedral angle coordinate. Analogous to the S_1/S_0 MESX, the T_1/S_0 MESX structures directed to the E (reactant) and Z (photoproduct) isomers are characterized by a twist of the vinyl double

bond (Figure S5), although to a lesser extent than found for the S_1/S_0 MESX. The relevant parameters and computed $T_1 \rightarrow S_0$ ISC rates k_{ISC} are given in Table 5. Under our experimental conditions, energy is conserved, implying that after ISC from the V($\pi\pi^*$) state to the triplet manifold, T_1 is populated with an excess energy of 1.6 eV. Following the equipartition theorem, such an excess energy corresponds to a temperature of 252 K. In combination with small $\Delta E^{\ddagger}$ values, this leads to a rate of $(5.0\ \mathrm{ns})^{-1}$, which –considering the sensitivity of the rate to the calculated parameters in equation (3)– agrees quite well with the experimentally observed rate of $(29\ \mathrm{ns})^{-1}$.

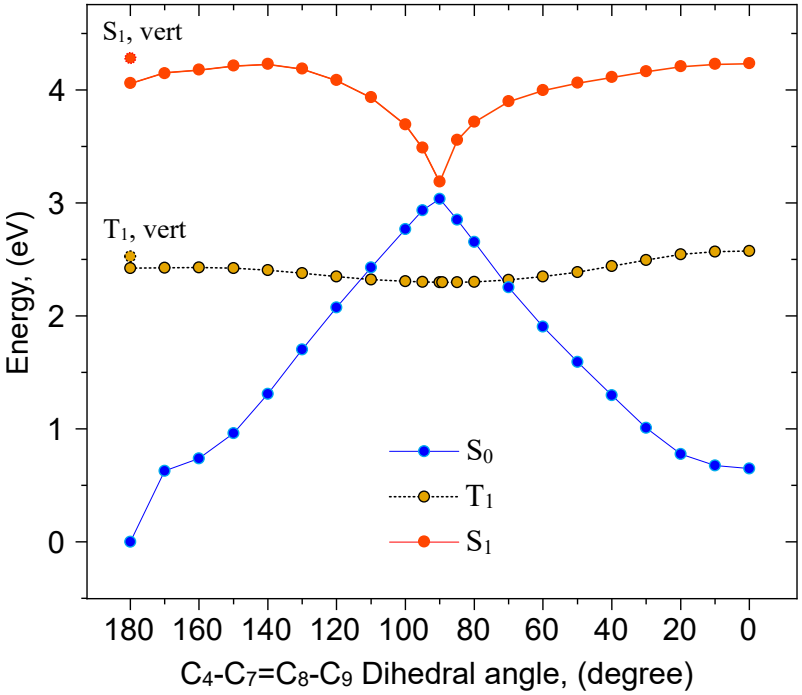

Figure 7: uDFT relaxed T_1 scan. Corresponding single-point singlet energies have been computed with TD-DFT at T_1 relaxed geometries. MESX structures appear on both sides of the twisted T_1 minimum, one to the E isomer (reactant) and one to the Z isomer (product).

The observation that in compounds based on cinnamate, coumarate, ferulate and sinapate chromophores very similar T_1 lifetimes are found may now be rationalized by noting that in all these molecules T_1 is the $V(^3\pi\pi^*)$ state, which is at a similar energy and characterized by an equilibrium geometry in which the initial vinyl double bond is considerably twisted

Table 5: Marcus parameters for $T_1 \rightarrow S_0$ ISC (Equation 3). SOCMEs evaluated at the uDFT optimized MESX geometries with TD-DFT energies. $\Delta E^{\ddagger}$ is based on the energy difference between the uDFT optimized MESX and uDFT optimized T_1 geometries. Rates computed at 252 K based on excess energy of 1.6 eV.

	$\langle T_1\|\hat{H}_{\mathrm{SO}}\|S_0\rangle$ (cm^{-1})	$\Delta E^{\ddagger}$ (eV)	λ (eV)	$(k_{\mathrm{ISC}})^{-1}$ (ns)	R2PI τ_2 (ns)
MESX,E	1.3	0.030	3.012	13.6	29
MESX,Z	1.3	0.019	2.875	8.0	

Table 6: Experimentally observed T_1 lifetimes and uDFT T_1 energies of MC, MF, and MS. For MC and MS, two energetically close geometrical T_1 structures were found.

Compound	$\tau(T_1)$ (ns)	T_1 (eV)
MC	29[36]	2.207 / 2.219[10]
MF	29	2.298
MS	27[29]	†2.107 / 2.123[37]

†Calculation was based on sinapic acid.

(Table 6). In order to obtain comparable k_{ISC} rates, however, $\Delta E^{\ddagger}$ and hence the T_1/S_0 MESX energies should be similar. Inspection of the HOMO and LUMO orbitals at the $T_1$and T_1/S_0 MESX geometries (Figure 8) shows that at both geometries the dominant part of the electron density is localized on the but-2-eonate part of the molecule. As a result, the substitution pattern on the phenyl ring is expected to be of minor influence on the energies of the T_1 state at these geometries.

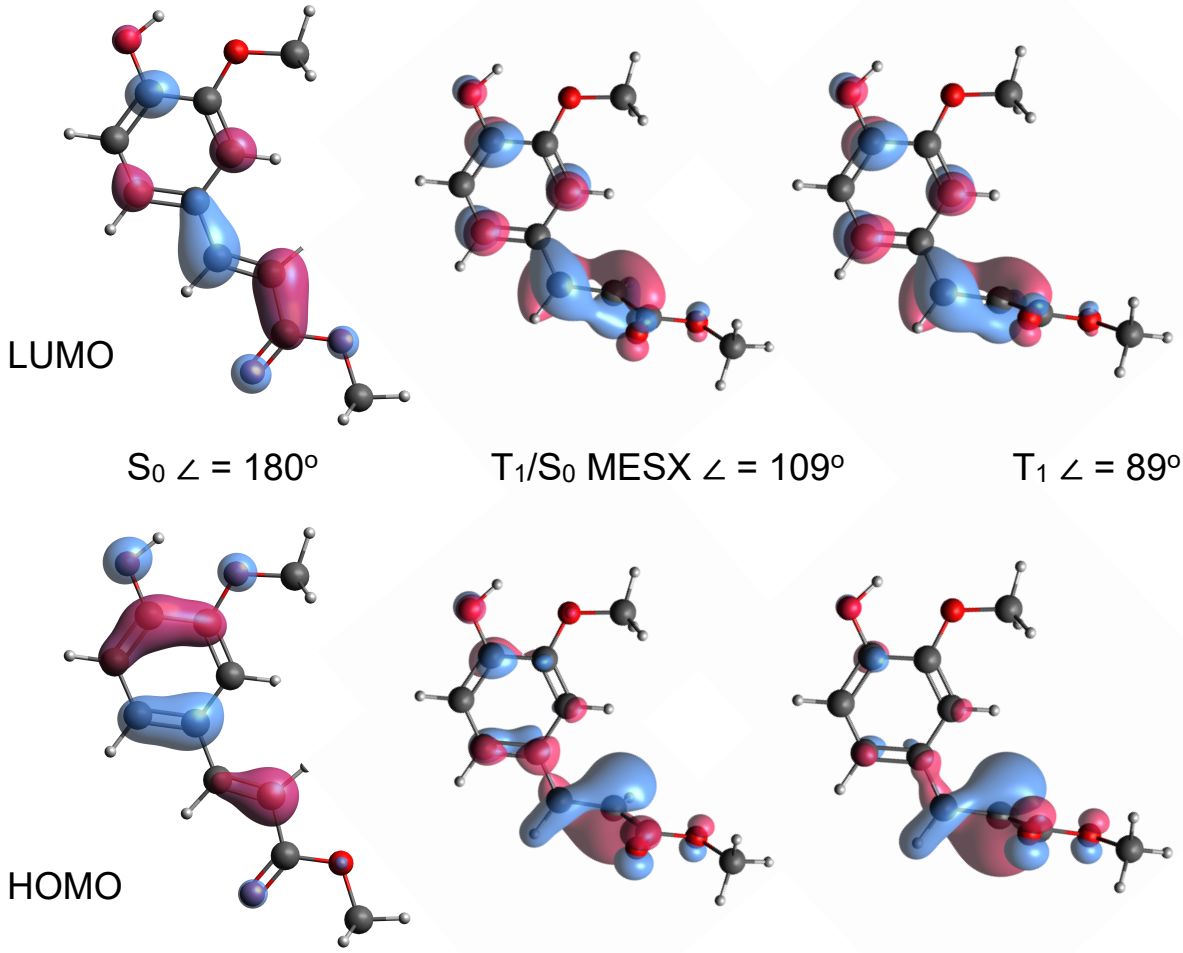

Figure 8: HOMO and LUMO orbitals of the *syn/cis* conformer of MF at S_0, T_1/S_0 MESX and T_1 optimized geometries. Indicated for each geometry is the C_4-C_7=C_8-C_9 dihedral angle.

4. Conclusions

Methyl ferulate can be considered as a prototypical compound in between coumarates and sinapates, two classes of nature-based UV filters with critically different electronically excited state manifolds. Studies of its electronically excited states and their dynamics are thus paramount to further our understanding of the changes imparted by substitutions of the cinnamate backbone. Furthermore, to connect to their real-life application it is crucial to

understand to what extent interactions with a solvent influence its properties.

In the present studies such information has been obtained by applying Resonance Enhanced MultiPhoton Ionization spectroscopic techniques on isolated and microsolvated compounds under molecular beam conditions in combination with quantum chemical calculations. Our studies demonstrate that the UV absorbing properties of MF are dominated by a bright $V(\pi\pi^*)$ state. Importantly, experiment and theory show that the intensity distribution over characteristic vibronic progression of an in-plane bending mode is highly conformation dependent. We find that water preferentially coordinates to the carbonyl group and in doing so, it red shifts the bright $V(\pi\pi^*)$ state. Interestingly, depletion-IR measurements lead to the conclusion that also clusters are generated in which water disrupts the intramolecular phenolic hydrogen bond, resulting in a blue shift of the phenolic OH stretch mode. Such clusters have a considerably higher energy but appear to be kinetically trapped during the expansion.

Our studies show that for low internal energies in the $V(\pi\pi^*)$ state the absorbed photon energy is dissipated along the routes summarized in Figure 9. Similar as in MS, the electron-donating ortho-methoxy group in MF raises the energy of the π-orbital, resulting in an adiabatic excited-state ordering that places the $V(\pi\pi^*)$ state below the $^1\mathrm{n}\pi^*$ state. As a result, the triplet manifold is populated through El-Sayed-forbidden $V(\pi\pi^*) \rightarrow T_2(\pi\pi^*)$ ISC, in contrast to MC, where rapid El-Sayed-allowed $^1n\pi^* \rightarrow T_1(\pi\pi^*)$ ISC takes place.[32] Fast ISC back to S_0 is made possible through a T_1/S_0 crossing mediated route. Importantly, because the electron density is dominantly localized at the but-2-enoate tail for transient structures close to the T_1/S_0 crossing very similar T_1 decay rates are observed for cinnamates and phenyl-substituted cinnamates, irrespective of the further substitution details. The initial slow ISC from the $V(\pi\pi^*)$ state in ferulates and sinapates is beneficial from a molecular heater point of view as triplet states are typically associated with photochemical degradation reactions. An additional advantage is that these compounds also have an efficient pathway of repopulating the ground state from T_1.

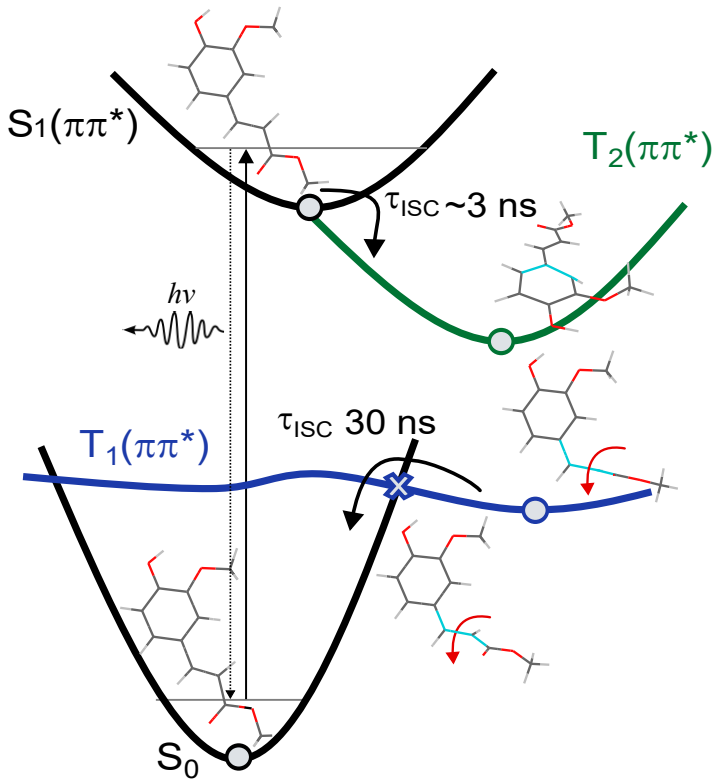

Figure 9: Summary of photophysical decay pathway of adiabatically excited MF. Geometries of relevant optimized structures are shown as well. Note the cyan colouring of some atoms to highlight certain molecular distortions. ISC to the T_2 state is followed by rapid internal conversion to T_1. A twisting motion forms a T_1/S_0 MESX, which leads to ISC back to the ground state.

The detailed insight that has been afforded by the present studies on the decay channels of electronically excited states in MF and related compounds breaks new ground for research into the design of highly efficient sunscreens and molecular heaters. Based on the present studies a number of potential interesting substitutions can be thought of that are currently further explored experimentally both under molecular beam as well as solution conditions.

Supporting Information

Additional computational results of adiabatic and vertical excitation energies at various levels, description of lower electronically excited singlet states, and relative energies of MF conformers. Additional computational results on OH-stretch frequencies and S_1 excitation

energies of MF-H_2O conformers. Predicted $V(\pi\pi^*) \leftarrow S_0$ excitation spectrum of *anti/cis* conformer of MF. Comparison UV-UV depletion spectra of *syn/cis* (a), *syn/trans* (c) and *anti/trans* (e) conformers of MF, and TD-DFT computed vibrationally-resolved excitation spectra of their *V'* state. IR-UV depletion spectra OH-stretch region MF conformers. Calculated equilibrium geometries lower-lying triplet states *syn/cis* MF, T_1/S_0 MESX structures of E (reactant) and Z (photoproduct) MF isomers. Coordinates of various structures of MF and MF-H_2O discussed in the text.

Acknowledgement

We thank ing. Michiel Hilbers and Dr. Wim Roeterdink for technical support. This project has received funding from the European Union's Horizon 2020 research and innovation programme under the grant agreement No. 828753 (Boostcrop). JMT and MB thank the European Research Council (ERC) Advanced grant SubNano (grant agreement 832237).

References

(1) Baker, L. A.; Marchetti, B.; Karsili, T. N. V.; Stavros, V. G.; Ashfold, M. N. R. Photoprotection: extending lessons learned from studying natural sunscreens to the design of artificial sunscreen constituents. *Chem. Soc. Rev.* **2017**, *46*, 3770–3791.

(2) Chenu, A.; Scholes, G. D. Coherence in Energy Transfer and Photosynthesis. *Annual Review of Physical Chemistry* **2015**, *66*, 69–96.

(3) Brixner, T.; Stenger, J.; Vaswani, H. M.; Cho, M.; Blankenship, R. E.; Fleming, G. R. Two-dimensional spectroscopy of electronic couplings in photosynthesis. *Nature* **2005**, *434*, 625–628.

(4) Roy, P.; Browne, W. R.; Feringa, B. L.; Meech, S. R. Ultrafast motion in a third generation photomolecular motor. *Nature Communications* **2023**, *14*, 1253.

(5) Schapiro, I.; Gueye, M.; Paolino, M.; Fusi, S.; Marchand, G.; Haacke, S.; Martin, M. E.; Huntress, M.; Vysotskiy, V. P.; Veryazov, V. et al. Synthesis, spectroscopy and QM/MM simulations of a biomimetic ultrafast light-driven molecular motor. *Photochemical & Photobiological Sciences* **2019**, *18*, 2259–2269.

(6) Wang, Z.; Roffey, A.; Losantos, R.; Lennartson, A.; Jevric, M.; Petersen, A. U.; Quant, M.; Dreos, A.; Wen, X.; Sampedro, D. et al. Macroscopic heat release in a molecular solar thermal energy storage system. *Energy Environ. Sci.* **2019**, *12*, 187–193.

(7) Abiola, T. T.; Rioux, B.; Toldo, J. M.; Alarcan, J.; Woolley, J. M.; Turner, M. A. P.; Coxon, D. J. L.; Telles do Casal, M.; Peyrot, C.; Mention, M. M. et al. Towards developing novel and sustainable molecular light-to-heat converters. *Chem. Sci.* **2021**, *12*, 15239–15252.

(8) Yamazaki, K.; Miyazaki, Y.; Harabuchi, Y.; Taketsugu, T.; Maeda, S.; Inokuchi, Y.; Kinoshita, S.-n.; Sumida, M.; Onitsuka, Y.; Kohguchi, H. et al. Multistep Intersystem Crossing Pathways in Cinnamate-Based UV-B Sunscreens. *The Journal of Physical Chemistry Letters* **2016**, *7*, 4001–4007, PMID: 27657500.

(9) Iida, Y.; Kinoshita, S.-n.; Kenjo, S.; Muramatsu, S.; Inokuchi, Y.; Zhu, C.; Ebata, T. Electronic States and Nonradiative Decay of Cold Gas-Phase Cinnamic Acid Derivatives Studied by Laser Spectroscopy with a Laser-Ablation Technique. *The Journal of Physical Chemistry A* **2020**, *124*, 5580–5589, PMID: 32551660.

(10) Kenjo, S.; Iida, Y.; Chaki, N.; nosuke Kinoshita, S.; Inokuchi, Y.; Yamazaki, K.; Ebata, T. Laser spectroscopic study on sinapic acid and its hydrated complex in a cold gas phase molecular beam. *Chemical Physics* **2018**, *515*, 381–386, Ultrafast Photoinduced Processes in Polyatomic Molecules:Electronic Structure, Dynamics and Spectroscopy (Dedicated to Wolfgang Domcke on the occasion of his 70th birthday).

(11) Liu, Y.; Zhao, X.; Luo, J.; Yang, S. Excited-state dynamics of sinapate esters in aqueous solution and polyvinyl alcohol film. *Journal of Luminescence* **2019**, *206*, 469–473.

(12) Dean, J. C.; Kusaka, R.; Walsh, P. S.; Allais, F.; Zwier, T. S. Plant Sunscreens in the UV-B: Ultraviolet Spectroscopy of Jet-Cooled Sinapoyl Malate, Sinapic Acid, and Sinapate Ester Derivatives. *Journal of the American Chemical Society* **2014**, *136*, 14780–14795, PMID: 25295994.

(13) Horbury, M. D.; Flourat, A. L.; Greenough, S. E.; Allais, F.; Stavros, V. G. Investigating isomer specific photoprotection in a model plant sunscreen. *Chem. Commun.* **2018**, *54*, 936–939.

(14) Horbury, M. D.; Turner, M. A. P.; Peters, J. S.; Mention, M.; Flourat, A. L.; Hine, N. D. M.; Allais, F.; Stavros, V. G. Exploring the Photochemistry of an Ethyl Sinapate

Dimer: An Attempt Toward a Better Ultraviolet Filter. *Frontiers in Chemistry* **2020**, *8*, 633.

(15) Baker, L. A.; Staniforth, M.; Flourat, A. L.; Allais, F.; Stavros, V. G. Gas-Solution Phase Transient Absorption Study of the Plant Sunscreen Derivative Methyl Sinapate. *ChemPhotoChem* **2018**, *2*, 743–748.

(16) Boeije, Y.; Olivucci, M. From a one-mode to a multi-mode understanding of conical intersection mediated ultrafast organic photochemical reactions. *Chem. Soc. Rev.* **2023**, *52*, 2643–2687.

(17) Abiola, T. T.; Toldo, J. M.; do Casal, M. T.; Flourat, A. L.; Rioux, B.; Woolley, J. M.; Murdock, D.; Allais, F.; Barbatti, M.; Stavros, V. G. Direct structural observation of ultrafast photoisomerization dynamics in sinapate esters. *Communications Chemistry* **2022**, *5*, 141.

(18) Toldo, J. M.; do Casal, M. T.; Barbatti, M. Mechanistic Aspects of the Photophysics of UVA Filters Based on Meldrum Derivatives. *The Journal of Physical Chemistry A* **2021**, *125*, 5499–5508, PMID: 34151555.

(19) Tan, E. M. M.; Hilbers, M.; Buma, W. J. Excited-State Dynamics of Isolated and Microsolvated Cinnamate-Based UV-B Sunscreens. *The Journal of Physical Chemistry Letters* **2014**, *5*, 2464–2468, PMID: 26277816.

(20) Miyazaki, Y.; Yamamoto, K.; Aoki, J.; Ikeda, T.; Inokuchi, Y.; Ehara, M.; Ebata, T. Experimental and theoretical study on the excited-state dynamics of ortho-, meta-, and para-methoxy methylcinnamate. *The Journal of Chemical Physics* **2014**, *141*, 244313.

(21) Stavros, V. G. A bright future for sunscreens. *Nature Chemistry* **2014**, *6*, 955–956.

(22) Peperstraete, Y.; Staniforth, M.; Baker, L. A.; Rodrigues, N. D. N.; Cole-Filipiak, N. C.;

Quan, W.-D.; Stavros, V. G. Bottom-up excited state dynamics of two cinnamate-based sunscreen filter molecules. *Phys. Chem. Chem. Phys.* **2016**, *18*, 28140–28149.

(23) Rodrigues, N. D. N.; Staniforth, M.; Stavros, V. G. Photophysics of sunscreen molecules in the gas phase: a stepwise approach towards understanding and developing next-generation sunscreens. *Proceedings of the Royal Society A* **2016**, *472*, 20160677.

(24) Maltseva, E.; Amirjalayer, S.; Buma, W. J. Vibrationally-resolved spectroscopic studies of electronically excited states of 1,8-naphthalic anhydride and 1,8-naphthalimide: a delicate interplay between one $\pi\pi^*$ and two $n\pi^*$ states. *Phys. Chem. Chem. Phys.* **2017**, *19*, 5861–5869.

(25) d. N. Rodrigues, N.; Stavros, V. G. From Fundamental Science to Product: A Bottom-up Approach to Sunscreen Development. *Science Progress* **2018**, *101*, 8–31, PMID: 29422118.

(26) Holt, E. L.; Stavros, V. G. Applications of ultrafast spectroscopy to sunscreen development, from first principles to complex mixtures. *International Reviews in Physical Chemistry* **2019**, *38*, 243–285.

(27) Liu, F.; Du, L.; Lan, Z.; Gao, J. Hydrogen bond dynamics governs the effective photoprotection mechanism of plant phenolic sunscreens. *Photochemical & Photobiological Sciences* **2017**, *16*, 211–219.

(28) Dalton, J.; Toldo, J. M.; Allais, F.; Barbatti, M.; Stavros, V. G. Understanding the Impact of Symmetrical Substitution on the Photodynamics of Sinapate Esters Using Gas-Phase Ultrafast Spectroscopy. *The Journal of Physical Chemistry Letters* **2023**, *14*, 8771–8779, PMID: 37738948.

(29) Fan, J.; Roeterdink, W.; Buma, W. J. Excited-state dynamics of isolated and (micro)solvated methyl sinapate: the bright and shady sides of a natural sunscreen. *Molecular Physics* **2021**, *119*, e1825850.

(30) Rodrigues, N. D. N.; Staniforth, M.; Young, J. D.; Peperstraete, Y.; Cole-Filipiak, N. C.; Gord, J. R.; Walsh, P. S.; Hewett, D. M.; Zwier, T. S.; Stavros, V. G. Towards elucidating the photochemistry of the sunscreen filter ethyl ferulate using time-resolved gas-phase spectroscopy. *Faraday Discuss.* **2016**, *194*, 709–729.

(31) Kinoshita, S.-n.; Inokuchi, Y.; Onitsuka, Y.; Kohguchi, H.; Akai, N.; Shiraogawa, T.; Ehara, M.; Yamazaki, K.; Harabuchi, Y.; Maeda, S. et al. The direct observation of the doorway 1nπ* state of methylcinnamate and hydrogen-bonding effects on the photochemistry of cinnamate-based sunscreens. *Phys. Chem. Chem. Phys.* **2019**, *21*, 19755–19763.

(32) Kinoshita, S.-n.; Harabuchi, Y.; Inokuchi, Y.; Maeda, S.; Ehara, M.; Yamazaki, K.; Ebata, T. Substitution effect on the nonradiative decay and trans → cis photoisomerization route: a guideline to develop efficient cinnamate-based sunscreens. *Phys. Chem. Chem. Phys.* **2021**, *23*, 834–845.

(33) Gromov, E.; Burghardt, I.; Köppel, H.; Cederbaum, L. Impact of sulfur vs oxygen on the low-lying excited states of *trans-p*-coumaric acid and *trans-p*-coumaric thio acid. *Journal of Physical Chemistry A* **2005**, *109*, 4623–4631.

(34) Tan, E. M. M.; Amirjalayer, S.; Bakker, B. H.; Buma, W. J. Excited state dynamics of Photoactive Yellow Protein chromophores elucidated by high-resolution spectroscopy and ab initio calculations. *Faraday Discuss.* **2013**, *163*, 321–340.

(35) de Groot, M.; Gromov, E. V.; Köppel, H.; Buma, W. J. High-Resolution Spectroscopy of Methyl 4-Hydroxycinnamate and Its Hydrogen-Bonded Water Complex. *The Journal of Physical Chemistry B* **2008**, *112*, 4427–4434, PMID: 18338881.

(36) Smolarek, S.; Vdovin, A.; Tan, E. M. M.; de Groot, M.; Buma, W. J. Spectroscopy and dynamics of methyl-4-hydroxycinnamate: the influence of isotopic substitution and water complexation. *Phys. Chem. Chem. Phys.* **2011**, *13*, 4393–4399.

(37) Kinoshita, S.-n.; Miyazaki, Y.; Sumida, M.; Onitsuka, Y.; Kohguchi, H.; Inokuchi, Y.; Akai, N.; Shiraogawa, T.; Ehara, M.; Yamazaki, K. et al. Different photoisomerization routes found in the structural isomers of hydroxy methylcinnamate. *Phys. Chem. Chem. Phys.* **2018**, *20*, 17583–17598.

(38) Fan, J.; Finazzi, L.; Buma, W. J. Elucidating the photoprotective properties of natural UV screening agents: ZEKE–PFI spectroscopy of methyl sinapate. *Phys. Chem. Chem. Phys.* **2022**, *24*, 3984–3993.

(39) Smolarek, S.; Vdovin, A.; Rijs, A.; van Walree, C. A.; Zgierski, M. Z.; Buma, W. J. High-Resolution Spectroscopy of Jet-Cooled 1,1'-Diphenylethylene: Electronically Excited and Ionic States of a Prototypical Cross-Conjugated System. *The Journal of Physical Chemistry A* **2011**, *115*, 9399–9410, PMID: 21332230.

(40) Grimme, S.; Waletzke, M. A combination of Kohn–Sham density functional theory and multi-reference configuration interaction methods. *The Journal of Chemical Physics* **1999**, *111*, 5645–5655.

(41) Marian, C. M.; Heil, A.; Kleinschmidt, M. The DFT/MRCI method. *WIREs Computational Molecular Science* **2019**, *9*, e1394.

(42) Computational Chemistry Comparison and Benchmark Database: Precomputed Vibrational Scaling Factors. `https://cccbdb.nist.gov/vibscalejust.asp`, 2020; Accessed August 2020.

(43) Frisch, M. J.; Trucks, G. W.; Schlegel, H. B.; Scuseria, G. E.; Robb, M. A.; Cheeseman, J. R.; Scalmani, G.; Barone, V.; Petersson, G. A.; Nakatsuji, H. et al. Gaussian˜16 Revision A.03. 2016; Gaussian Inc. Wallingford CT.

(44) Ahlrichs, R.; Bär, M.; Häser, M.; Horn, H.; Kölmel, C. Electronic structure calculations on workstation computers: The program system turbomole. *Chemical Physics Letters* **1989**, *162*, 165–169.

(45) Kleinschmidt, M.; Marian, C. M.; Waletzke, M.; Grimme, S. Parallel multireference configuration interaction calculations on mini-β-carotenes and β-carotene. *The Journal of Chemical Physics* **2009**, *130*, 044708.

(46) Levine, B. G.; Coe, J. D.; Martínez, T. J. Optimizing Conical Intersections without Derivative Coupling Vectors: Application to Multistate Multireference Second-Order Perturbation Theory (MS-CASPT2). *The Journal of Physical Chemistry B* **2008**, *112*, 405–413, PMID: 18081339.

(47) Heß, B. A.; Marian, C. M.; Wahlgren, U.; Gropen, O. A mean-field spin-orbit method applicable to correlated wavefunctions. *Chemical Physics Letters* **1996**, *251*, 365–371.

(48) Gao, X.; Bai, S.; Fazzi, D.; Niehaus, T.; Barbatti, M.; Thiel, W. Evaluation of Spin-Orbit Couplings with Linear-Response Time-Dependent Density Functional Methods. *Journal of Chemical Theory and Computation* **2017**, *13*, 515–524, PMID: 27959528.

(49) Smolarek, S.; Vdovin, A.; Perrier, D. L.; Smit, J. P.; Drabbels, M.; Buma, W. J. High-Resolution Excitation and Absorption Spectroscopy of Gas-Phase *p*-Coumaric Acid: Unveiling an Elusive Chromophore. *Journal of the American Chemical Society* **2010**, *132*, 6315–6317, PMID: 20397707.

(50) Tan, E. M. M. Structural Dynamics of Isolated Biological and Synthetic Photoswitches. Ph.D. thesis, Universiteit van Amsterdam, 2011; [Thesis, fully internal].

(51) Herkstroeter, W. G.; Farid, S. Photodimerization — relevant triplet state parameters of methyl cinnamate, diethyl 1,4-phenylenediacrylate and methyl 1-naphthylacrylate. *Journal of Photochemistry* **1986**, *35*, 71–85.

(52) Brédas, J.-L.; Beljonne, D.; Coropceanu, V.; Cornil, J. Charge-Transfer and Energy-Transfer Processes in π-Conjugated Oligomers and Polymers: A Molecular Picture. *Chemical Reviews* **2004**, *104*, 4971–5004, PMID: 15535639.

(53) El-Sayed, M. A. Triplet state. Its radiative and nonradiative properties. *Accounts of Chemical Research* **1968**, *1*, 8–16.

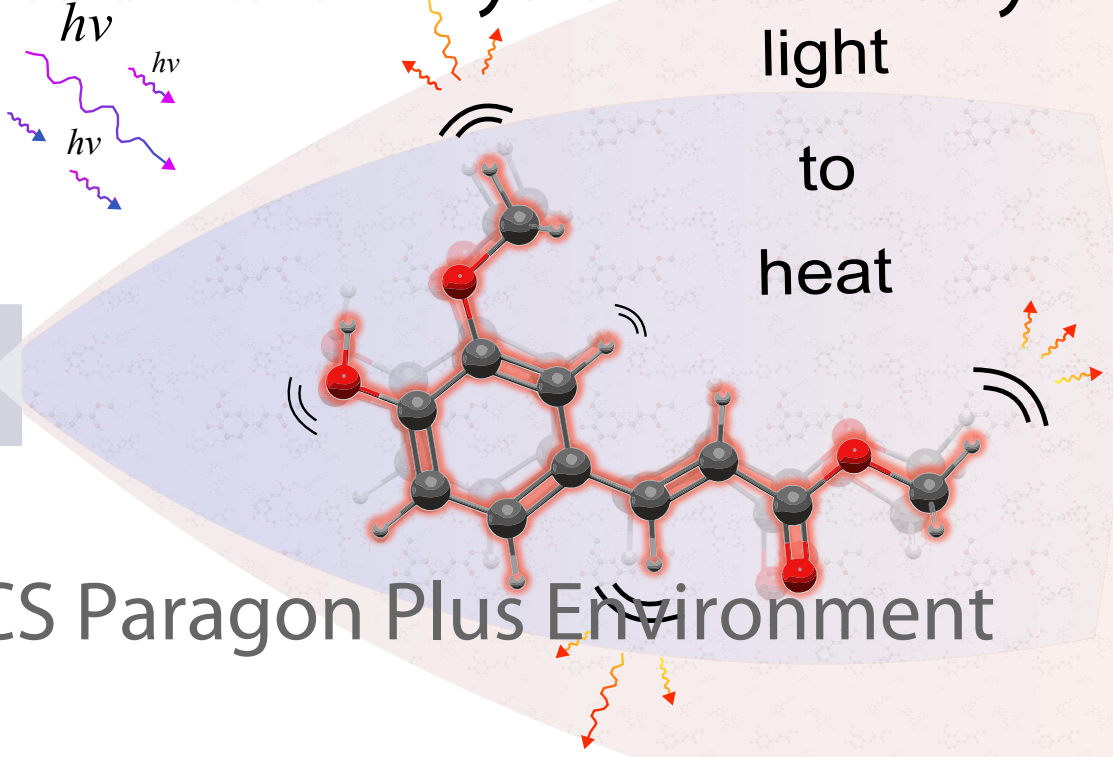

1
2
3
4
5
6
7